

Fully-gapped superconducting state in interstitial-carbon-doped Zr_5Pt_3

T. Shang,^{1,*} J. Philippe,^{2,†} X. Y. Zhu,¹ H. Zhang,¹ B. C. Yu,¹ Z. X. Zhen,¹ H.-R. Ott,² J. Kitagawa,³ and T. Shiroka^{2,4,‡}

¹Key Laboratory of Polar Materials and Devices (MOE), School of Physics and Electronic Science, East China Normal University, Shanghai 200241, China

²Laboratorium für Festkörperphysik, ETH Zürich, CH-8093 Zurich, Switzerland

³Department of Electrical Engineering, Fukuoka Institute of Technology, Fukuoka 811-0295, Japan

⁴Laboratory for Muon-Spin Spectroscopy, Paul Scherrer Institut, CH-5232 Villigen PSI, Switzerland

We report a comprehensive study of the $\text{Zr}_5\text{Pt}_3\text{C}_x$ superconductors, with interstitial carbon comprised between 0 and 0.3. At a macroscopic level, their superconductivity, with T_c ranging from 4.5 to 6.3 K, was investigated via electrical-resistivity-, magnetic-susceptibility-, and specific-heat measurements. The upper critical fields $\mu_0 H_{c2} \sim 7$ T were determined mostly from measurements of the electrical resistivity in applied magnetic fields. The microscopic electronic properties were investigated by means of muon-spin rotation and relaxation (μSR) and nuclear magnetic resonance (NMR) techniques. In the normal state, NMR relaxation data indicate an almost ideal metallic behavior, confirmed by band-structure calculations, which suggest a relatively high electronic density of states at the Fermi level, dominated by the Zr 4d orbitals. The low-temperature superfluid density, obtained via transverse-field μSR , suggests a fully-gapped superconducting state in Zr_5Pt_3 and $\text{Zr}_5\text{Pt}_3\text{C}_{0.3}$, with a zero-temperature gap $\Delta_0 = 1.20$ and 0.60 meV and a magnetic penetration depth $\lambda_0 = 333$ and 493 nm, respectively. The exponential dependence of the NMR relaxation rates below T_c further supports a nodeless superconductivity. The absence of spontaneous magnetic fields below the onset of superconductivity, as determined from zero-field μSR measurements, confirms a preserved time-reversal symmetry in the superconducting state of $\text{Zr}_5\text{Pt}_3\text{C}_x$. In contrast to a previous study, our μSR and NMR results suggest a conventional superconductivity in the $\text{Zr}_5\text{Pt}_3\text{C}_x$ family, independent of the C content.

I. INTRODUCTION

The T_5M_3 family, where T is a d -transition or rare-earth metal and M a (post)-transition metal or a metalloid element, features three distinct structural symmetries: orthorhombic Yb_5Sb_3 -type ($Pnma$, No. 62), tetragonal Cr_5B_3 -type ($I4/mcm$, No. 140), and hexagonal Mn_5Si_3 -type ($P6_3/mcm$, No. 193). The Cr_5B_3 -type structure is adopted by a broad range of binary and ternary compounds, e.g., the layered ternary compounds of transition metals with boron and silicon, with a $T_5\text{XB}_2$ stoichiometry ($X = \text{P}$ or Si), known to exhibit many interesting properties. For $T = 3d$ -Mn or Fe, both $T_5\text{SiB}_2$ and $T_5\text{PB}_2$ are ferromagnets with Curie temperatures above 480 and 600 K, respectively. Hence, currently they are being considered for room-temperature magnetocaloric applications or as rare-earth-free permanent magnets [1–4]. For $T = 4d$ -Nb, Mo, or $5d$ -Ta, W metals, all $T_5\text{SiB}_2$ are superconductors, with transition temperatures in the 5 to 8 K range [5–8]. Furthermore, the recently synthesized tetragonal Mo_5PB_2 was shown to exhibit multigap superconductivity (SC) with a critical temperature $T_c = 9.2$ K [9, 10], the highest T_c recorded in a Cr_5B_3 -type compound.

The hexagonal Mn_5Si_3 -type structure possesses an interstitial $2b$ site, well suited for the intercalation of light elements, such as oxygen, boron, or carbon, employed to engineer the band topology and, ultimately, the electronic properties. Superconductivity has been reported in several families of materials, including $\text{Nb}_5\text{Ir}_3\text{O}_x$ [11], $(\text{Nb,Zr})_5\text{Pt}_3\text{O}$ [12, 13], $\text{Nb}_5\text{Ge}_3\text{C}_x$ [14, 15], or $\text{Zr}_5\text{Pt}_3\text{C}_x$ [16], with the highest superconducting transition temperature T_c reaching ~ 15 K. Upon intercalation of oxygen [11], the T_c of Nb_5Ir_3 increases up to 10.5 K, while upon Pt doping, a crossover from multiple to single-gap SC occurs in $\text{Nb}_5\text{Ir}_{3-x}\text{Pt}_x\text{O}$ [17, 18]. Contrary

to the $\text{Nb}_5\text{Ir}_3\text{O}_x$ case, in Zr_5Pt_3 or Zr_5Sb_3 , the addition of oxygen reduces the T_c value [13, 19].

In carbon-intercalated $\text{Zr}_5\text{Pt}_3\text{C}_x$, the T_c value depends nonmonotonically on x , first increasing up to 7 K for $x = 0.3$, then decreasing to ~ 4 K, as the amount of intercalated C is further increased [16, 20]. The first electronic specific-heat and magnetic penetration-depth studies suggested that Zr_5Pt_3 and $\text{Zr}_5\text{Pt}_3\text{C}_{0.3}$ are nodal superconductors, implying their unconventional SC character [16]. However, recent muon-spin rotation and relaxation (μSR) results are consistent with a conventional s -wave pairing in $\text{Zr}_5\text{Pt}_3\text{C}_{0.5}$ [20]. More intriguingly, the theoretical calculations predict $\text{Zr}_5\text{Pt}_3\text{C}_x$ to be Dirac nodal-line semimetals and, as such, good candidates for realizing topological SC [20].

Although the superconductivity of $\text{Zr}_5\text{Pt}_3\text{C}_x$ compounds has been investigated by magnetic- and transport measurements, complemented by electronic band-structure calculations, the microscopic nature of their SC is still not well established. Moreover, the lack of a shared doping makes the conclusions of the previous studies regarding the superconducting pairing in $\text{Zr}_5\text{Pt}_3\text{C}_x$ inconsistent and hardly comparable [16, 20]. To clarify these issues, we synthesized a series of $\text{Zr}_5\text{Pt}_3\text{C}_x$ ($x = 0\text{--}0.3$) samples, and systematically studied their superconducting properties by means of electrical resistivity, magnetization, and heat-capacity measurements, complemented by μSR and nuclear magnetic resonance (NMR) methods. We find that $\text{Zr}_5\text{Pt}_3\text{C}_x$ exhibits a fully-gapped superconducting state with a preserved time-reversal symmetry. Our detailed local-probe results suggest a conventional s -wave SC in the $\text{Zr}_5\text{Pt}_3\text{C}_x$ family, essentially independent of the C content.

II. EXPERIMENTAL DETAILS

Polycrystalline $\text{Zr}_5\text{Pt}_3\text{C}_x$ ($x = 0\text{--}0.3$) samples were prepared by arc melting the Zr and C powders and Pt wires with different stoichiometric ratios in a high-purity argon atmosphere. Zr and C powders were firstly mixed and pressed into

* These authors contributed equally; Corresponding author:

tshang@phy.ecnu.edu.cn

† These authors contributed equally

‡ Corresponding author:

tshiroka@phys.ethz.ch

pellets. The ZrC-pellets and Pt wires were then arc melted. To improve the homogeneity, the samples were flipped and remelted several times and were then annealed under vacuum conditions at 800°C over 4 days. Room-temperature x-ray powder diffraction (XRD) measurements were used to check the crystal structure and phase purity of the $\text{Zr}_5\text{Pt}_3\text{C}_x$ samples, by employing a Shimadzu (XRD-7000) diffractometer. The magnetic-susceptibility-, electrical-resistivity-, and heat-capacity measurements were performed using a Quantum Design MPMS and PPMS system. The bulk μSR measurements were carried out at the multipurpose surface-muon spectrometer (Dolly) of the Swiss muon source at the Paul Scherrer Institut in Villigen, Switzerland. Both transverse-field (TF) and zero-field (ZF) μSR measurements were performed. As to the former, they allowed us to determine the temperature evolution of the superfluid density. As to the latter, we aimed at searching for a possible breaking of time-reversal symmetry in the superconducting state of $\text{Zr}_5\text{Pt}_3\text{C}_x$. To exclude the possibility of stray magnetic fields during the ZF- μSR measurements, all the magnets were preliminarily degaussed. All the μSR spectra were collected upon heating and were analyzed by means of the *musrfit* software package [21].

A series of ^{195}Pt NMR measurements on powdered $\text{Zr}_5\text{Pt}_3\text{C}_x$ samples in a magnetic field of 4.011 T provided the line shapes and the spin-lattice relaxation times. We used a continuous-flow CF-1200 cryostat by Oxford Instruments to cover the 2 to 300 K temperature range, with temperatures below 4.2 K being reached under pumped ^4He conditions. The ^{195}Pt reference frequency was determined from the ^{27}Al resonance, scaled by using the NMR frequency tables [22]. The ^{195}Pt NMR signal was detected by means of a standard spin-echo sequence consisting of $\pi/2$ and π pulses of 6 and 12 μs , with recycling delays ranging from 0.1 to 2 s in the 2–300 K temperature range. Spin-lattice relaxation times T_1 were measured via the inversion-recovery method, using a $\pi-\pi/2-\pi$ pulse sequence with phase cycling for minimizing possible artifacts. The powder samples were used for the x-ray diffraction, magnetization, μSR , and NMR measurements, while the electrical-resistivity and heat capacity measurements were performed on the cut slabs.

III. RESULTS AND DISCUSSION

A. Crystal structure

The crystal structure and the purity of $\text{Zr}_5\text{Pt}_3\text{C}_x$ ($x = 0-0.3$) polycrystalline samples was checked via XRD at room temperature. The XRD patterns shown in Fig. 1(a) confirm that all of them share the same hexagonal Mn_5Si_3 -type structure, with no discernible traces of foreign phases (see details in Fig. S1 in the Supplemental Material (SM) [23]). As an example, the crystal structure of $\text{Zr}_5\text{Pt}_3\text{C}_x$ for $x = 1$ is shown in the inset of Fig. 1(b). When $x < 1$, the occupation of the $2b$ sites is less than 1. We note that, for $x > 0.5$, sizeable amounts of secondary phases (mostly ZrPt) appear [16, 20]. Thus, here we investigate $\text{Zr}_5\text{Pt}_3\text{C}_x$ samples with $x \leq 0.3$. The lattice parameters of each sample were obtained by the least-squares method and the results are summarized in Fig 1(b). Upon increasing the C-content, a decreases slightly, from 8.182(3) Å (for $x = 0$) to 8.167(4) Å (for $x = 0.3$), while c increases from 5.384(2) Å (for $x = 0$) to 5.390(3) Å (for $x = 0.3$). In the Zr_5Pt_3 parent compound, we obtain lattice parameters consistent with previous reports [13, 16].

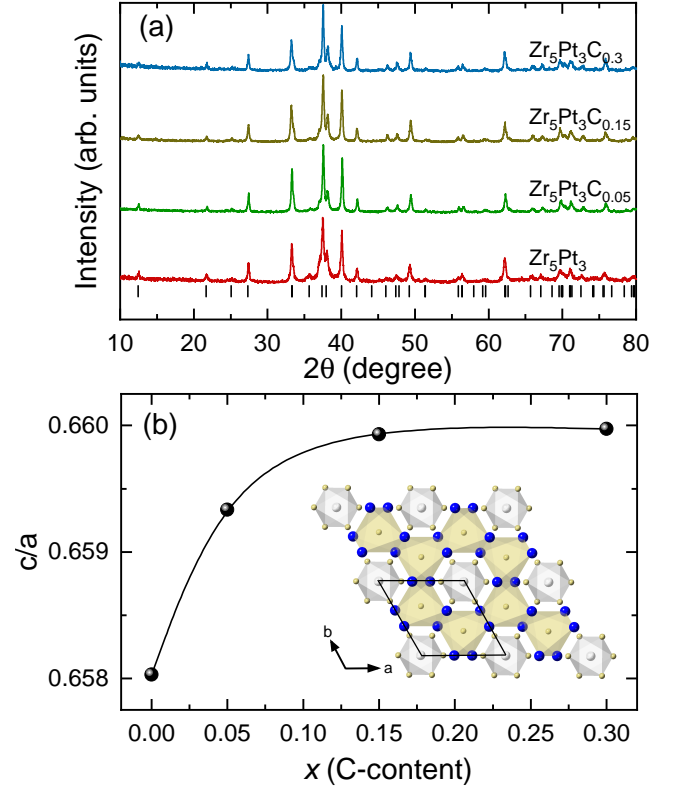


FIG. 1. (a) Room-temperature x-ray powder diffraction patterns for $\text{Zr}_5\text{Pt}_3\text{C}_x$ ($x = 0-0.3$). The vertical bars mark the calculated Bragg-peak positions for Zr_5Pt_3 with a space group $P6_3/mcm$. (b) The c/a ratio versus the C-content. The inset shows the crystal structure of $\text{Zr}_5\text{Pt}_3\text{C}$ viewed along the c axis (solid lines mark the unit cell). Blue, yellow, and gray spheres represent the Pt, Zr, and C atoms, respectively.

However, for the C-intercalated samples, the parameter sets differ. In particular, in a previous study, c was found to be almost independent of x , while a was reported to increase with x , resulting in a gradual suppression of the c/a ratio [16]. In our samples, instead, the c/a ratio increases upon increasing x , to saturate at $x > 0.15$ [see Fig. 1(b)]. Compared to the previous results, our samples show a better crystalline quality, reflected in much sharper XRD reflections in Fig. 1(a). The reason for such discrepant results for $\text{Zr}_5\text{Pt}_3\text{C}_x$ is not yet clear and requires further investigation.

B. Superconducting temperature and lower critical field H_{c1}

The temperature dependence of the electrical resistivity $\rho(T)$, collected in zero magnetic field, reveals the metallic character of $\text{Zr}_5\text{Pt}_3\text{C}_x$ ($x = 0-0.3$). The electrical resistivity in the low- T region (below 10 K) is shown in Fig. 2(a). For Zr_5Pt_3 , the superconducting transition, with $T_c^{\text{onset}} = 7.2$ K, $T_c^{\text{mid}} = 6.8$ K, and $T_c^{\text{zero}} = 6.1$ K is clearly visible and the T_c s are consistent with previous results [16]. Here T_c^{mid} indicates the temperature at the middle of superconducting transition. When intercalating carbon into the Zr_5Pt_3 structure, T_c is reduced, with $T_c^{\text{onset}} = 5.2$ K, $T_c^{\text{mid}} = 4.9$ K, and $T_c^{\text{zero}} = 4.4$ K in $\text{Zr}_5\text{Pt}_3\text{C}_{0.3}$. The slightly different T_c values between the current and the previous work are most likely attributed to a different actual carbon content [16, 20]. Since our intercalated samples exhibit almost identical T_c values with varying C content, our μSR and NMR measurements focused on $\text{Zr}_5\text{Pt}_3\text{C}_x$ with $x = 0$ and 0.3.

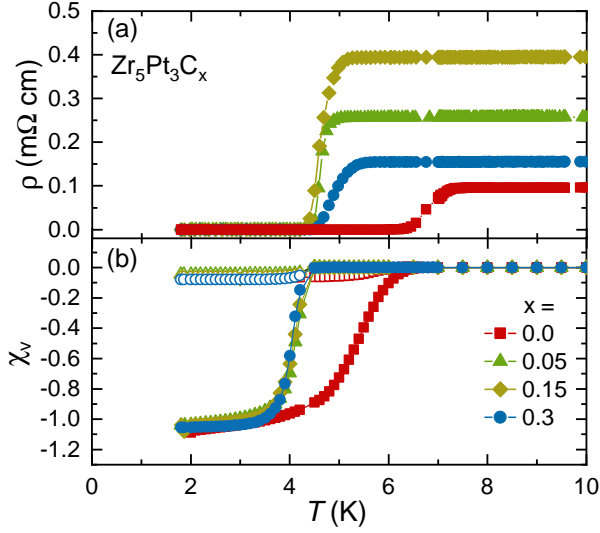


FIG. 2. Temperature-dependent electrical resistivity $\rho(T)$ (a) and magnetic susceptibility $\chi_v(T)$ (b) for C-intercalated $\text{Zr}_5\text{Pt}_3\text{C}_x$. While $\rho(T)$ was measured in a zero-field condition, $\chi_v(T)$ data were collected in a magnetic field of 1 mT using both the ZFC and FC protocols. The magnetic susceptibilities were corrected by considering the demagnetization factor obtained from the field-dependent magnetization at 2 K (base temperature).

The superconductivity of $\text{Zr}_5\text{Pt}_3\text{C}_x$ was further characterized by magnetic susceptibility measurements, using both field-cooled (FC) and zero-field-cooled (ZFC) protocols in an applied field of 1 mT. As shown in Fig. 2(b), a clear diamagnetic signal appears below the superconducting transition at $T_c = 6.3$ and 4.5 K for Zr_5Pt_3 and $\text{Zr}_5\text{Pt}_3\text{C}_{0.3}$, respectively, in agreement with the values determined from electrical resistivity in Fig. 2(a). After accounting for the demagnetization factor, the superconducting shielding fraction of $\text{Zr}_5\text{Pt}_3\text{C}_x$ samples is almost 100%, indicative of bulk SC. To determine the lower critical field H_{c1} , essential for performing μSR measurements on type-II superconductors, the field-dependent magnetization $M(H)$ was collected at various temperatures up to T_c . As an example, some representative $M(H)$ curves are shown in Fig. 3(a) for Zr_5Pt_3 . The C-intercalated samples exhibit very similar features. The resulting H_{c1} values as a function of temperature are summarized in Fig. 3(b) for $\text{Zr}_5\text{Pt}_3\text{C}_x$. As shown by solid lines, the estimated zero-temperature H_{c1} values are $\mu_0 H_{c1}(0) = 5.5(1), 3.8(1), 4.4(1),$ and $4.4(1)$ mT for $x = 0, 0.05, 0.15,$ and 0.3 , respectively. The different H_{c1} values of Zr_5Pt_3 and $\text{Zr}_5\text{Pt}_3\text{C}_{0.3}$ are consistent with the magnetic penetration depth determined from TF- μSR measurements (see below).

C. Upper critical field H_{c2}

The upper critical fields H_{c2} of $\text{Zr}_5\text{Pt}_3\text{C}_x$ were determined from measurements of the electrical resistivity $\rho(T, H)$ in various applied magnetic fields. As an example, the $\rho(T, H)$ curves of Zr_5Pt_3 and $\text{Zr}_5\text{Pt}_3\text{C}_{0.3}$ are shown in Figs. 4(a) and 4(b), respectively. In an applied field, the superconducting transition shifts toward lower temperatures and broadens. For $\text{Zr}_5\text{Pt}_3\text{C}_{0.3}$, as shown in the inset of Fig. 4(b), also specific-heat measurements in various magnetic fields were performed. Since, for $x = 0.3$, the T_c values determined from the specific heat $C(T, H)/T$ coincide with T_c^{zero} determined from the electrical-resistivity measurements [see Fig. 5(d)],

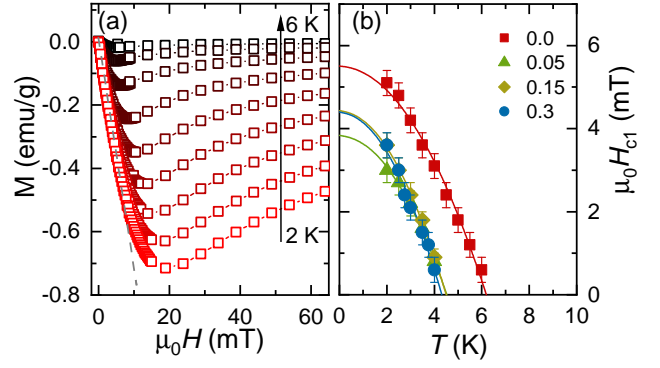


FIG. 3. (a) Field-dependent magnetization $M(H)$ recorded at various temperatures up to T_c for Zr_5Pt_3 . (b) Lower critical fields H_{c1} vs temperature for $\text{Zr}_5\text{Pt}_3\text{C}_x$ ($x = 0-0.3$). The solid lines represent fits to $\mu_0 H_{c1}(T) = \mu_0 H_{c1}(0)[1 - (T/T_c)^2]$. For each temperature, the lower critical field H_{c1} was determined as the value where $M(H)$ starts deviating from linearity (indicated by the dashed line).

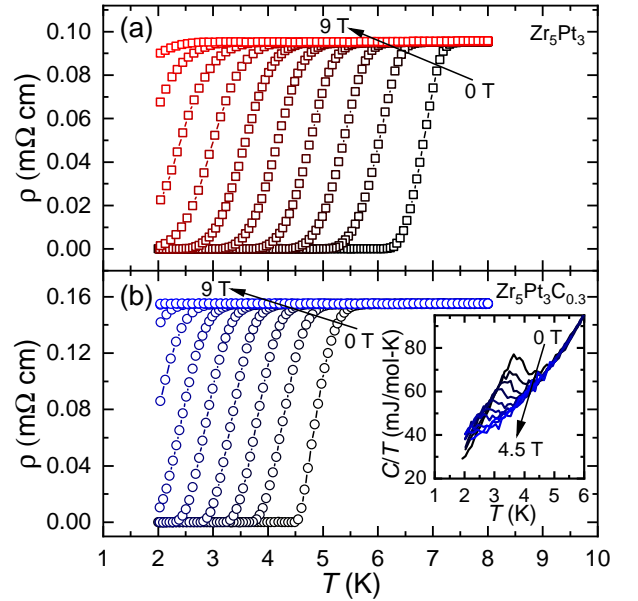


FIG. 4. Temperature-dependent electrical resistivity $\rho(T, H)$ collected at various magnetic fields up to 9 T for Zr_5Pt_3 (a) and $\text{Zr}_5\text{Pt}_3\text{C}_{0.3}$ (b). Inset of (b): Temperature-dependent specific heat $C(T, H)/T$ collected at various magnetic fields up to 4.5 T. In $\rho(T, H)$ measurements, T_c was determined as the onset of the zero electrical resistivity, i.e., T_c^{zero} , while in $C(T, H)/T$ measurements, T_c was defined as the midpoint of the superconducting transition. The resulting T_c values are summarized in the H - T phase diagram shown in Fig. 5.

we used the T_c^{zero} values as a criterion to determine $H_{c2}(0)$ for all the $\text{Zr}_5\text{Pt}_3\text{C}_x$ samples. The $H_{c2}(T)$ vs $T_c/T_c(0)$ data [here, $T_c(0)$ is the transition temperature in zero field] are summarized in Fig. 5. Each $H_{c2}(T)$ curve was analyzed by means of Ginzburg-Landau (GL), $H_{c2} = H_{c2}(0)(1 - t^2)/(1 + t^2)$, [24] and Werthamer-Helfand-Hohenberg (WHH) models [25]. As shown by the dash-dotted lines, the WHH model can describe the $H_{c2}(T)$ data reasonably well up to 2 T. However, at higher magnetic fields, this model deviates significantly from the experimental data and provides underestimated H_{c2} values. By contrast, as shown by the solid lines in Fig. 5, the GL model agrees remarkably well with the experimental data and provides $\mu_0 H_{c2}(0) = 7.21(5), 6.26(4), 6.42(9),$ and $6.97(6)$ T for $x = 0, 0.05, 0.15,$ and 0.3 , respectively.

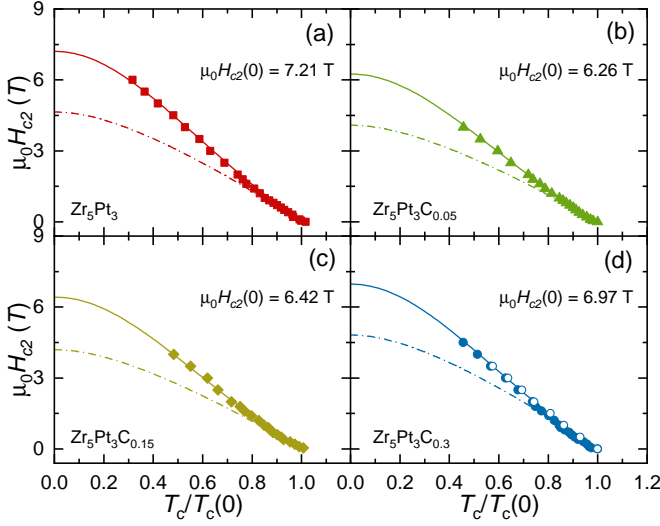


FIG. 5. Upper critical field H_{c2} vs the reduced transition temperature $T_c/T_c(0)$ for Zr_5Pt_3 (a), $\text{Zr}_5\text{Pt}_3\text{C}_{0.05}$ (b), $\text{Zr}_5\text{Pt}_3\text{C}_{0.15}$ (c), and $\text{Zr}_5\text{Pt}_3\text{C}_{0.3}$ (d). The T_c values were determined from measurements shown in Fig. 4. For $\text{Zr}_5\text{Pt}_3\text{C}_{0.3}$, the T_c values determined from $C(T,H)/T$ (open symbols) are consistent with the values determined from $\rho(T,H)$ (closed symbols). The solid and dash-dotted lines represent fits to the GL- and WHH-models.

In the GL theory of superconductivity, the magnetic penetration depth λ is related to the coherence length ξ , and the lower critical field via $\mu_0 H_{c1} = (\Phi_0/4\pi\lambda^2)[\ln(\kappa) + \alpha(\kappa)]$, where $\Phi_0 = 2.07 \times 10^{-3} \text{ T } \mu\text{m}^2$ is the quantum of magnetic flux, $\kappa = \lambda/\xi$ is the GL parameter, and $\alpha(\kappa)$ is a parameter which converges to 0.497 for $\kappa \gg 1$ [26]. By using $\mu_0 H_{c1}$ and ξ values [calculated from $\mu_0 H_{c2}(0) = \Phi_0/2\pi\xi(0)^2$], the resulting $\lambda_{\text{GL}} = 366(4)$ and $415(6)$ for Zr_5Pt_3 and $\text{Zr}_5\text{Pt}_3\text{C}_{0.3}$ are compatible with the experimental value determined from μSR data. All the superconducting parameters are summarized in Table I. A GL parameter $\kappa \gg 1$ confirms again that $\text{Zr}_5\text{Pt}_3\text{C}_x$ are type-II superconductors.

D. μSR study

1. Transverse-field μSR

To investigate Zr_5Pt_3 and $\text{Zr}_5\text{Pt}_3\text{C}_{0.3}$ at a microscopic level, we carried out systematic TF- μSR measurements in an applied field of 30 mT, i.e., more than twice their H_{c1} values [see Fig. 3(b)]. Representative TF- μSR spectra collected in the superconducting and normal states of Zr_5Pt_3 and $\text{Zr}_5\text{Pt}_3\text{C}_{0.3}$ are shown in Figs. 6(a) and 6(b), respectively. For both compounds, the normal-state spectra show essentially no damping, thus reflecting the uniform field distribution, as well as the lack of magnetic impurities. In the superconducting state (below T_c), instead, the significantly enhanced damping reflects the inhomogeneous field distribution due to the development of a flux-line lattice (FLL) [27–30]. The broadening of the field distribution is clearly visible in Figs. 6(c) and 6(d), where the fast-Fourier transform (FFT) spectra of the corresponding TF- μSR data of Zr_5Pt_3 are presented. To describe the asymmetric field distribution [e.g., see FFT at 0.3 K in Fig. 6(c)], the TF- μSR spectra were

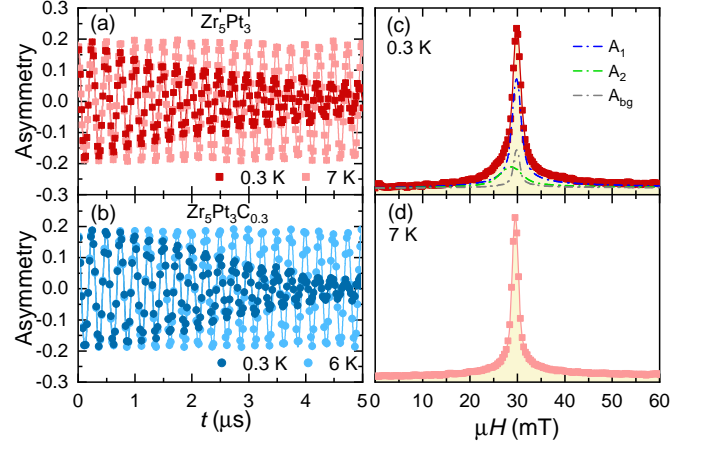


FIG. 6. TF- μSR spectra collected in the normal and superconducting states in an applied magnetic field of 30 mT for Zr_5Pt_3 (a) and $\text{Zr}_5\text{Pt}_3\text{C}_{0.3}$ (b). Fast Fourier transforms of the TF- μSR data shown in (a) at 0.3 K (c) and at 7 K (d). For Zr_5Pt_3 , solid lines are fits to Eq. (1) using two oscillations, which are also shown separately as dash-dotted lines in (c), together with a background contribution. For $\text{Zr}_5\text{Pt}_3\text{C}_{0.3}$, solid lines are fits to Eq. (1) with a single oscillation. Note the clear field-distribution broadening due to FLL below T_c .

modeled using

$$A_{\text{TF}}(t) = \sum_{i=1}^n A_i \cos(\gamma_\mu B_i t + \phi) e^{-\sigma_i^2 t^2/2} + A_{\text{bg}} \cos(\gamma_\mu B_{\text{bg}} t + \phi). \quad (1)$$

Here A_i , A_{bg} and B_i , B_{bg} are the initial asymmetries and local fields sensed by implanted muons in the sample and sample holder (copper, which normally shows zero muon-spin depolarization), $\gamma_\mu/2\pi = 135.53 \text{ MHz/T}$ is the muon gyromagnetic ratio, ϕ is a shared initial phase, and σ_i is the Gaussian relaxation rate of the i th component. Generally, the field distribution in the superconducting state is material dependent: the more asymmetric it is, the more components are required to describe it. Here, we find that, while two oscillations (i.e., $n = 2$) are required to properly describe the TF- μSR spectra of Zr_5Pt_3 , a single oscillation is sufficient for $\text{Zr}_5\text{Pt}_3\text{C}_{0.3}$. For Zr_5Pt_3 , the dash-dotted lines in Fig. 6(c) represent the two components at 0.3 K (A_1 and A_2) and the background signal (A_{bg}). Above T_c , the muon-spin relaxation rate is small and temperature-independent, but below T_c it starts to increase due to the onset of FLL and the increased superfluid density. At the same time, a diamagnetic field shift, $\Delta B(T) = \langle B \rangle - B_{\text{appl}}$, appears below T_c , with $\langle B \rangle = (A_1 B_1 + A_2 B_2)/A_{\text{tot}}$, $A_{\text{tot}} = A_1 + A_2$, and $B_{\text{appl}} = 30 \text{ mT}$ (see insets in Fig. 7). The effective Gaussian relaxation rate can be calculated from $\sigma_{\text{eff}}^2/\gamma_\mu^2 = \sum_{i=1}^2 A_i [\sigma_i^2/\gamma_\mu^2 - (B_i - \langle B \rangle)^2]/A_{\text{tot}}$ [30]. Then, the superconducting Gaussian relaxation rate σ_{sc} , can be extracted by subtracting the nuclear contribution according to $\sigma_{\text{sc}} = \sqrt{\sigma_{\text{eff}}^2 - \sigma_n^2}$. Here, σ_n is the nuclear relaxation rate, almost constant in the covered temperature range and extremely small for $\text{Zr}_5\text{Pt}_3\text{C}_x$, as confirmed also by ZF- μSR data (see Fig. 8). At low magnetic fields ($H_{\text{appl}}/H_{c2} \sim 0.004 \ll 1$), the effective magnetic penetration depth λ_{eff} and, thus, the superfluid density $\rho_{\text{sc}} (\propto \lambda_{\text{eff}}^{-2})$, can be calculated using $\sigma_{\text{sc}}^2(T)/\gamma_\mu^2 = 0.00371 \Phi_0^2/\lambda_{\text{eff}}^4(T)$ [26, 31].

The superfluid density ρ_{sc} of Zr_5Pt_3 and $\text{Zr}_5\text{Pt}_3\text{C}_{0.3}$ vs the reduced temperature T/T_c is shown in Figs. 7(a) and 7(b), respectively. In both cases, the temperature-invariant superfluid density below $T_c/3$ suggests the absence of low-energy

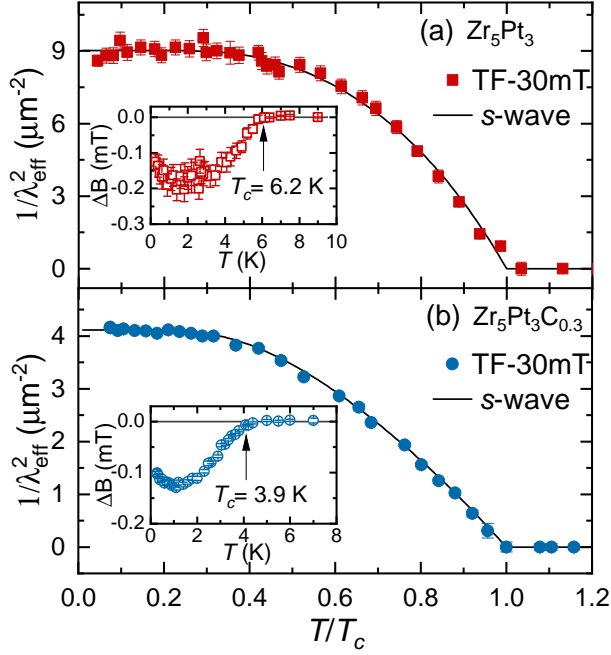


FIG. 7. Superfluid density vs reduced temperature T/T_c for Zr_5Pt_3 (a) and $\text{Zr}_5\text{Pt}_3\text{C}_{0.3}$ (b). Insets show the diamagnetic shift $\Delta B(T)$. The solid lines in the main panels represent fits to a fully gapped s -wave model with a single energy gap.

excitations and, hence, a fully-gapped superconducting state. Consequently, the $\rho_{sc}(T)$ was analyzed by means of a fully-gapped s -wave model:

$$\rho_{sc}(T) = \frac{\lambda_{eff}^{-2}(T)}{\lambda_0^{-2}} = 1 + 2 \int_{\Delta(T)}^{\infty} \frac{\partial f}{\partial E} \frac{E dE}{\sqrt{E^2 - \Delta^2(T)}}. \quad (2)$$

Here, $f = (1 + e^{E/k_B T})^{-1}$ is the Fermi function; $\Delta(T)$ is the superconducting-gap function, assumed to follow $\Delta(T) = \Delta_0 \tanh\{1.82[1.018(T_c/T - 1)]^{0.51}\}$ [32, 33]; λ_0 and Δ_0 are the magnetic penetration depth and the superconducting gap at 0 K, respectively. As shown by the solid lines in Fig. 7, the s -wave model describes $\rho_{sc}(T)$ very well across the entire temperature range with the fit parameters: $\Delta_0 = 1.20(2)$ and $0.60(2)$ meV, and $\lambda_0 = 333(3)$ and $493(2)$ nm for Zr_5Pt_3 and $\text{Zr}_5\text{Pt}_3\text{C}_{0.3}$, respectively. The gap value and the magnetic penetration depth of $\text{Zr}_5\text{Pt}_3\text{C}_{0.3}$ are close to those of $\text{Zr}_5\text{Pt}_3\text{C}_{0.5}$ [20]. We considered also the dirty-limit model [32], which turned out to describe fairly well the $\rho_{sc}(T)$ of Zr_5Pt_3 and $\text{Zr}_5\text{Pt}_3\text{C}_{0.3}$, yielding slightly lower superconducting gap values (see details in Table I).

2. Zero-field μ SR

To verify the possible breaking of time-reversal symmetry in $\text{Zr}_5\text{Pt}_3\text{C}_{0.3}$, we also performed ZF- μ SR measurements in both its normal- and superconducting states. As shown in Fig. 8, neither coherent oscillations nor fast decays could be identified in the spectra collected above (10 K) and below T_c (2 K and 0.3 K), hence implying the lack of any magnetic order or fluctuations. The weak muon-spin relaxation in absence of an external magnetic field is mainly due to the randomly oriented nuclear moments, which can be modeled by a Gaussian Kubo-Toyabe relaxation function, $G_{KT} = [\frac{1}{3} + \frac{2}{3}(1 - \sigma_{ZF}^2 t^2) e^{-\sigma_{ZF}^2 t^2/2}]$ [27, 34]. Here,

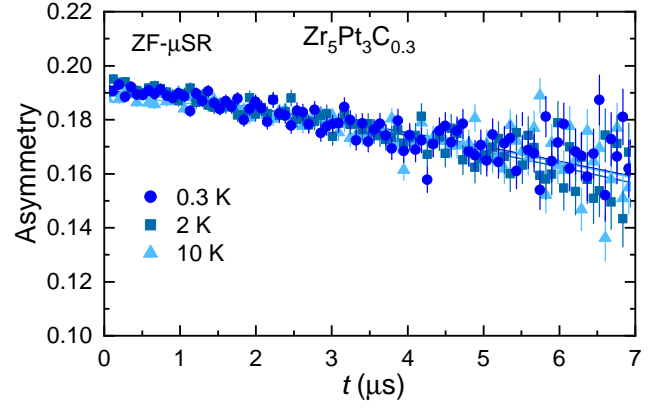


FIG. 8. Representative ZF- μ SR spectra in the normal (10 K) and the superconducting state (0.3 and 2 K) of $\text{Zr}_5\text{Pt}_3\text{C}_{0.3}$. Solid lines are fits to the equation described in the text. None of the datasets shows noticeable changes with temperature, suggesting the absence of spontaneous magnetic fields in the superconducting state.

σ_{ZF} is the zero-field Gaussian relaxation rate. The solid lines in Fig. 8 represent fits to the data by considering also an additional zero-field Lorentzian relaxation Λ_{ZF} , i.e., $A_{ZF}(t) = A_s G_{KT} e^{-\Lambda_{ZF} t} + A_{bg}$. The relaxation rates in the normal- and the superconducting states are almost identical, as confirmed by the practically overlapping ZF- μ SR spectra above and below T_c . The resulting relaxations at 0.3 K are listed in Table I. This lack of evidence for an additional μ SR relaxation below T_c excludes a possible time-reversal symmetry breaking in the superconducting state of $\text{Zr}_5\text{Pt}_3\text{C}_{0.3}$.

E. ^{195}Pt -NMR study

$\text{Zr}_5\text{Pt}_3\text{C}_x$ samples contain three NMR-active nuclei, i.e., ^{13}C , ^{91}Zr , and ^{195}Pt . However, the 1.1% isotopic abundance of ^{13}C , together with the low carbon content of the samples and its omnipresence in the probehead, made it difficult to use the ^{13}C NMR signal of $\text{Zr}_5\text{Pt}_3\text{C}_x$. The low-frequency, low-abundance ^{91}Zr , associated with its quadrupole effects ($I = 5/2$) made it unsuitable, too. Consequently, in the current work, we focus on the ^{195}Pt NMR results. A representative full-frequency scan is shown in Fig. S2, while the frequency ranges covered at low- T are listed in Table S1 of SM [23].

1. Static electronic properties: Knight shift

The ^{195}Pt NMR lineshapes (see Fig. S3 in SM [23]) were recorded by a standard spin-echo sequence and successively fitted with the `Dmfit` software [35]. By assuming a purely Gaussian profile for the spin-1/2 nuclei, we determined the precise peak positions and line widths. The Pt atoms reside in 6g sites [16] and are bonded in a 9-coordinate geometry to Zr atoms. Since the latter occupy two inequivalent sites (6g and 4d), of which the first with a 9% spread in Pt-Zr distances, relatively wide ^{195}Pt NMR lines are expected. Due to the large width of the lines, the shifts appear as small (see Fig. S3 [23]). Yet, numerical fits provide shift values typical of metallic compounds (i.e., a fraction of percent). As shown in Fig. 9, in the normal state, both Zr_5Pt_3 and $\text{Zr}_5\text{Pt}_3\text{C}_{0.3}$ exhibit a temperature-independent frequency shift (known as Knight shift, K) and linewidth (full width at half maximum, Γ_{FWHM}). In Zr_5Pt_3 (red symbols), we find $K = 0.195\%$ and

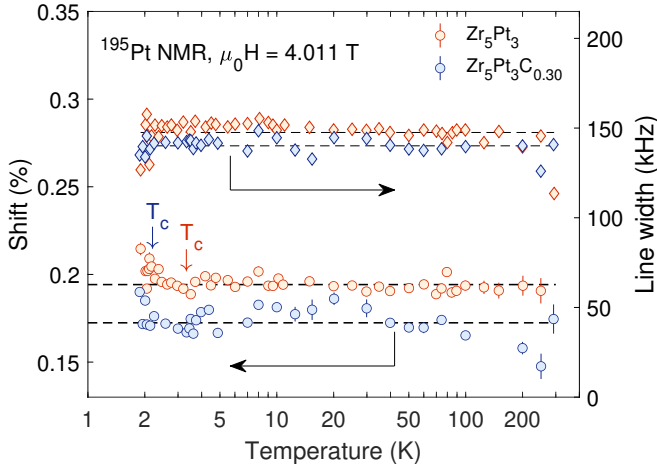


FIG. 9. ^{195}Pt NMR frequency shift (left scale) and linewidth (right scale) as function of temperature. In the normal state, both parameters are constant with temperature. Below T_c , we observe an increase in shift (see text for details). The arrows mark the T_c values.

$\Gamma_{\text{FWHM}} = 150$ kHz, while in $\text{Zr}_5\text{Pt}_3\text{C}_{0.3}$ (blue symbols) these values are 10% and 5% lower, respectively.

Similar features (i.e., wide lines, small and/or positive shifts, and no temperature dependence) have been reported also in NiPtP metallic glasses [36] or in Pt-Mo alloys [37]. These are to be compared with the -3.5% ^{195}Pt shift in elemental metallic Pt, whose large negative value is known to arise from a dominant core-polarization contribution [38]. In Mott's two-band ($s + d$) model, the density of states of the narrow d -band is much greater than that of the much wider s -band. Hence, any property which depends on the electronic density of states will, in general, be dominated by the unfilled d -band. In our case, the resulting positive increase in ^{195}Pt Knight shift provides evidence that the Pt d -states are filled, consistent with a charge transfer from Zr to the transition-metal atoms (we recall that Pt is twice as electronegative as Zr on the Pauling scale). In addition, the wide ^{195}Pt NMR linewidths, besides a distribution of atomic environments, suggest also a distribution in the degree of the d -state filling. In our case, it is precisely this type of filling which lowers the d character (and reduces the orbital effects), hence accounting for the positive NMR shift we observe. Of course, for quantitative results one has to consider also the spin-orbit, exchange correlation, and s - d hybridization effects [39, 40].

The orbital Knight shift, here preponderant and temperature independent, not only justifies our normal-state results, but also explains why the change in shift in the superconducting phase is so small. The increase in shift with decreasing temperature, we observe below T_c , is surprising. A possible reason for this might be the locally higher magnetic field at the SC vortex cores (see further). A similar behavior has been reported, e.g., in V_3Ga [41], where it was attributed to a significant reduction of the spin susceptibility. Independently of sign, a change in K across T_c represents a clear fingerprint of a fully-gapped conventional SC in $\text{Zr}_5\text{Pt}_3\text{C}_x$.

2. Dynamic electronic properties: Relaxation rates

In the superconducting state, the spin-lattice relaxation rates T_1^{-1} follow a thermally-activated behavior (see Fig. 10),

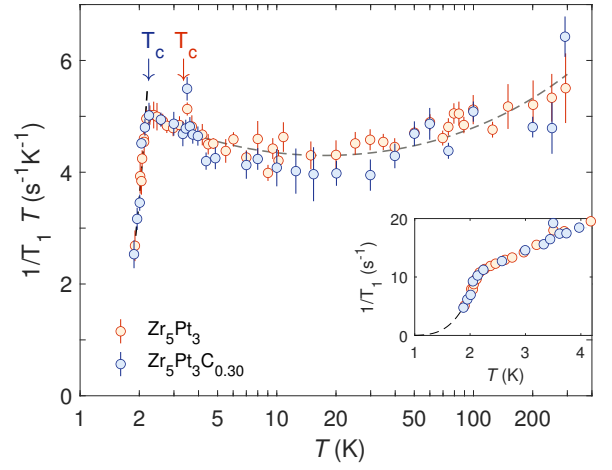


FIG. 10. $(T_1 T)^{-1}$ vs. T for the pure and C-doped Zr_5Pt_3 samples. Two fits are proposed: normal state (gray dashed line) and superconducting state (black dashed line). Inset: T_1^{-1} for $T \leq 4.2$ K; Fit of the thermally-activated relaxation rate (black dashed line). The initial unchanged trend below T_c might be due to the relaxation of nuclei inside the vortex cores. The arrows mark the T_c values determined from NMR shift in Fig. 9. The details of T_1 measurements and their analysis can be found in Figs. S4-S5 of SM [23].

whereas at temperatures above T_c , both samples exhibit an almost linearly dependent $T_1^{-1}(T)$ (see inset in Fig. 11). Since both samples exhibit almost identical relaxation rates across the whole temperature range, this implies that carbon doping does not significantly affect the relaxation mechanisms, here dominated by electronics fluctuations related to the Pt and Zr atoms. Note that the absence of a clear anomaly in $T_1^{-1}(T)$ curves near the onset of SC for both compounds is most likely attributed to their broad superconducting transition. In the normal state, the temperature-dependent spin-lattice relaxation rates $T_1^{-1}(T)$ provide useful insights into the dynamics of conduction electrons and their degree of correlations. Above T_c , $T_1^{-1}(T)$ deviates from a purely linear temperature dependence, clearly highlighted by the $(T_1 T)^{-1}$ vs T plot in Fig. 10, an indication of weak- to moderate electron correlations. In a first approximation, the estimated value of $(T_1 T)^{-1}$ at low temperature is about $4.72 \text{ s}^{-1}\text{K}^{-1}$. By a comparison to diborides, such as, MgB_2 , AlB_2 , and ZrB_2 (also binary superconductors [42]), this value indicates a relatively high electron density of states at the Fermi level (here dominated by the Zr and Pt d bands).

Now we discuss the NMR relaxation rates in the superconducting state. In an s -wave superconductor, the opening of an electronic energy gap below T_c implies an exponential decay of the NMR relaxation rate T_1^{-1} [43]:

$$T_1^{-1} \propto \exp\left(-\frac{\Delta_0}{k_B T}\right). \quad (3)$$

Here, Δ_0 is the same as in Eq. (2). In the superconducting state, after a slight initial enhancement, most likely due to the relaxation of nuclei inside the vortex cores [44], T_1^{-1} decreases exponentially and is described very well by Eq. (3) for both Zr_5Pt_3 and $\text{Zr}_5\text{Pt}_3\text{C}_{0.3}$. It is worth noting that, at 0 K, it converges towards zero (see inset in Fig. 10), thus suggesting that the electronic spin fluctuations represent the dominant relaxation channel (reflecting the exponential decrease of unpaired electrons in superconducting phase). This result also indicates the high quality of the samples (i.e., a negligible concentration of impurities and a 100% SC

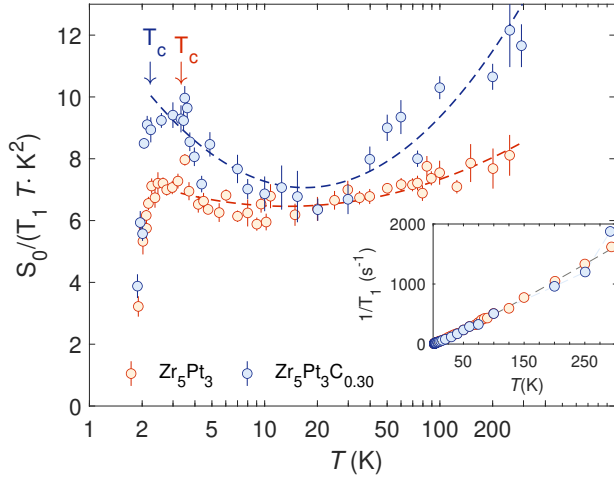


FIG. 11. The Korringa ratio S_0/S (expressed as $1/\alpha$) is always above unity. Here, $S_0/S > 1$ indicates the presence non- s -type hyperfine interactions. Inset: the spin-lattice relaxation rate. The arrows mark the T_c values determined from NMR shift in Fig. 9.

volume fraction). At the same time, spin fluctuations might account for the drop in signal intensity (wipeout effect [45]) we observe below T_c (see Fig. S6 in SM).

The superconducting gaps Δ_0 derived from Eq. (3) are listed in Table I. The gap sizes are slightly different from the TF- μ SR results, most likely related to the limited temperature range we can cover with our NMR setup. Although a coherence (Hebel-Slichter, HS) peak [46] just below T_c is a fingerprint of s -wave superconductivity, its absence not necessarily rules it out. Many factors may account for the suppression of the HS peak (as discussed in more detail in Ref. 47), but here we attribute it to the relevant contribution of d orbitals at the Fermi level.

Finally, we consider the degree of electron correlation in the normal state which, in an ideal-metal case, can be deduced from the Korringa relation [48]:

$$S = T_1 T K_s^2 = \alpha S_0, \quad \text{with} \quad S_0 = \frac{\gamma_e^2}{\gamma_n^2} \frac{\hbar}{4\pi k_B}, \quad (4)$$

where S is the Korringa constant, γ_e is the gyromagnetic ratio of free electrons, and γ_n that of the probe nucleus. We recall that, the total Knight shift K comprises both a spin- K_s and a (constant) orbital part K_{orb} . In case of a dominant K_s , arising from the Fermi-contact (i.e., momentum-independent) interaction associated with the Pauli susceptibility χ_p , the Korringa relation implies an α close to 1. As shown in Fig. 11, apart from a weak temperature dependence due to $T_1(T)$, both compounds exhibit Korringa constants lower than S_0 (note that, in Fig. 11, we report S_0/S on the y-axis). Clearly, the assumption of an s -type Fermi-contact interaction, required for the validity of the Korringa relation, is not fulfilled in our case. By accounting for the Pines corrections [49] to Eq. (4) (which include the terms $1/\rho^2(E_F)$ and χ_p^2 , reflecting the real density of states and spin susceptibility), we infer that the real $\rho(E_F)$ due to s electrons is less than expected. This suggests that the relaxation has a substantial orbital character, proportional to the density of d -states at the Fermi level, but otherwise the correlation is low. Therefore, we expect Zr_5Pt_3 and $\text{Zr}_5\text{Pt}_3\text{C}_{0.3}$ to be weakly correlated metals, despite a seemingly small S value.

IV. DISCUSSION

First, we discuss why our $\text{Zr}_5\text{Pt}_3\text{C}_x$ samples show a different evolution of T_c with C-content compared to a previous study, where the T_c values first increase from 6 K (for $x = 0$) to 7 K (for $x = 0.3$). Then, upon further increasing the C-content, T_c decreases continuously to 3.5 K (for $x = 0.7$) [16]. In our case, conversely, T_c decreases to 4.5 K already upon a 5% C intercalation (i.e., $x = 0.05$). Then, upon further increasing the C-content, T_c remains almost constant with x . Such a different evolution of T_c might be due to a carbon content differing from the nominal one, implying slightly different modifications of the crystal structure. In the previous study, upon C intercalation, the lattice was found to expand in the ab -plane, but to compress along the c -axis, resulting in a progressive decrease of the c/a ratio. This is also the case of the $\text{Nb}_5\text{Ir}_{3-x}\text{Pt}_x\text{O}$ family, where a smaller c/a ratio leads to a higher T_c value [17]. Our $\text{Zr}_5\text{Pt}_3\text{C}_x$ samples, instead, show an opposite behavior, with the c/a ratio increasing with C-content [see Fig. 1(b)]. Why our $\text{Zr}_5\text{Pt}_3\text{C}_x$ samples show a different lattice evolution compared to the previous work is not yet clear and requires further investigation.

Second, in the previous study, the temperature-dependent electronic specific heat and magnetic penetration depth (calculated from the lower critical field H_{c1}) suggest a nodal superconducting gap in Zr_5Pt_3 and $\text{Zr}_5\text{Pt}_3\text{C}_{0.3}$ and possibly unconventional SC [16]. However, both measurements were limited to ~ 2 K, i.e., only down to $1/3T_c$. To reliably reveal the superconducting pairing, measurements at temperatures far below the onset of SC (i.e., at $T < 1/3T_c$) are crucial, which is also one of the motivations of our study. Therefore, the original conclusion about unconventional SC in $\text{Zr}_5\text{Pt}_3\text{C}_x$ is not solid. This is clearly demonstrated in Fig. S7 of SM [23], where we show the magnetic penetration depth λ vs the reduced temperature T/T_c for $\text{Zr}_5\text{Pt}_3\text{C}_{0.3}$, both for our sample and for that reported in Ref. 16. As can be clearly seen, the $\lambda(T)$ determined from TF- μ SR shows an exponential temperature dependence below $1/3T_c$. For an isotropic single-gap superconductor, the magnetic penetration depth at $T \ll T_c$ follows $\lambda(T) - \lambda_0 = \lambda_0 \sqrt{\frac{\pi\Delta_0}{2T}} e^{-\frac{\Delta_0}{T}}$ [50], where λ_0 and Δ_0 are the same as in Eq. (2). The solid line in Fig. S7 [23] is a fit to the above equation, yielding a similar superconducting gap size as that determined from superfluid density $\rho_{\text{sc}}(T)$ in Fig. 7. The inset in Fig. S7 [23] replots the λ vs. $(T/T_c)^2$. As indicated by the dash-dotted lines, both data sets exhibit a T^2 dependence down to $T/T_c \sim 0.3$, while below it, $\lambda(T)$ deviates significantly from the T^2 dependence, decreasing exponentially with temperature, consistent with a fully-gapped SC state. We expect also the electronic specific heat to exhibit a similar exponential behavior, although currently the relevant low-temperature data are not yet available. To conclude, the limited temperature range of the previous experimental data might lead to an incorrect conclusion about the nature of SC [16]. By contrast, our TF- μ SR measurements, performed down to 0.3 K, i.e., well inside the SC state, combined with NMR results, prove beyond reasonable doubt the conventional character of $\text{Zr}_5\text{Pt}_3\text{C}_x$ superconductivity.

Third, the μ SR and NMR data of Zr_5Pt_3 and $\text{Zr}_5\text{Pt}_3\text{C}_{0.3}$ presented here, together with the previous study on $\text{Zr}_5\text{Pt}_3\text{C}_{0.5}$, suggest that the conventional SC of $\text{Zr}_5\text{Pt}_3\text{C}_x$ is independent of carbon content. Unlike the $\text{Nb}_5\text{Ir}_{3-x}\text{Pt}_x\text{O}$ family, where a crossover from multiple- to single-gap SC is observed upon

Table I. Normal- and superconducting-state properties of Zr_5Pt_3 and $\text{Zr}_5\text{Pt}_3\text{C}_{0.3}$, as determined from electrical-resistivity-, magnetization-, heat-capacity-, NMR-, and μSR measurements. The data for $\text{Zr}_5\text{Pt}_3\text{C}_{0.5}$ were taken from Ref. 20.

Property	Unit	Zr_5Pt_3	$\text{Zr}_5\text{Pt}_3\text{C}_{0.3}$	$\text{Zr}_5\text{Pt}_3\text{C}_{0.5}$
ρ_0	$\text{m}\Omega\text{ cm}$	0.095	0.155	—
T_c^{ρ}	K	6.1	4.4	3.8
T_c^{χ}	K	6.3	4.5	3.8
T_c^C	K	—	4.1	3.9
$T_c^{\mu\text{SR}}$	K	6.2	3.9	3.7
$\mu_0 H_{c1}$	mT	5.5(1)	4.4(1)	5.9
$\mu_0 H_{c1}^{\mu\text{SRa}}$	mT	6.5(1)	3.2(1)	3.4
$\mu_0 H_{c2}$	T	7.21(5)	6.97(6)	5.4
$\Delta_0^{\mu\text{SRb}}$	meV	1.20(2)	0.60(2)	0.59
$\Delta_0^{\mu\text{SRc}}$	meV	1.17(2)	0.47(2)	—
Δ_0^{NMR}	meV	0.98(8)	1.08(8)	—
$\xi(0)$	nm	6.10(3)	6.25(2)	7.81
κ	—	61	67	60
λ_0	nm	333(3)	493(2)	469
$\lambda_{\text{GL}}(0)$	nm	366(4)	415(6)	—
$\Lambda_{\text{ZF}}(0.3\text{ K})$	μs^{-1}	—	0.018(2)	—
$\sigma_{\text{ZF}}(0.3\text{ K})$	μs^{-1}	—	0.046(8)	—
$\Lambda_{\text{ZF}}(10\text{ K})$	μs^{-1}	—	0.015(4)	—
$\sigma_{\text{ZF}}(10\text{ K})$	μs^{-1}	—	0.048(8)	—

^a Calculated by $\mu_0 H_{c1} = (\Phi_0/4\pi\lambda^2)[\ln(\kappa) + 0.497]$.

^b Derived from clean-limit model.

^c Derived from dirty-limit model.

Pt doping [17, 18], here, the single-gap SC in $\text{Zr}_5\text{Pt}_3\text{C}_x$ is robust against the intercalation of interstitial carbon atoms. This is most likely attributed to their similar electronic band

structures. According to DFT calculations, up to six bands cross the Fermi level [20]. The density of states (DOS) is dominated by Zr d -orbitals (up to 68% of the total DOS, the rest being due to Pt), while the contribution of C p -orbitals is negligible. Moreover, the change in DOS is only about 10%, even when increasing the C-content up to $x = 1$.

V. CONCLUSION

To summarize, we investigated the normal- and superconducting properties of $\text{Zr}_5\text{Pt}_3\text{C}_x$ ($x = 0\text{--}0.3$) family of compounds by means of electrical resistivity-, magnetization-, heat capacity-, μSR , and NMR measurements. The $\text{Zr}_5\text{Pt}_3\text{C}_x$ exhibit bulk SC with T_c between 4.5 K and 6.3 K. The electrical-resistivity measurements under applied magnetic field reveal a zero-temperature upper critical field of ~ 7 T. The temperature dependence of the superfluid density reveals a *nodeless* SC in $\text{Zr}_5\text{Pt}_3\text{C}_x$, well described by an isotropic s -wave model. The conventional nature of $\text{Zr}_5\text{Pt}_3\text{C}_x$ superconductivity is also supported by the exponential temperature-dependent NMR relation rate and the change of Knight shift below T_c . Finally, the lack of spontaneous magnetic fields below T_c indicates that the time-reversal symmetry is preserved in the $\text{Zr}_5\text{Pt}_3\text{C}_x$ superconductors.

ACKNOWLEDGMENTS

This work was supported from the Natural Science Foundation of Shanghai (Grant Nos. 21ZR1420500 and 21JC1402300) and the Schweizerische Nationalfonds zur Förderung der Wissenschaftlichen Forschung (SNF) (Grant Nos. 200021_188706 and 206021_139082). We acknowledge the allocation of beam time at the Swiss muon source, and thank the scientists of Dolly μSR spectrometer for their support.

-
- [1] D. M. de Almeida, C. Bormio-Nunes, C. A. Nunes, A. A. Coelho, and G. C. Coelho, Magnetic characterization of Mn_5SiB_2 and Mn_5Si_3 phases, *J. Magn. Magn. Mater.* **321**, 2578 (2009).
 - [2] Z. G. Xie, D. Y. Geng, and Z. D. Zhang, Reversible room-temperature magnetocaloric effect in Mn_5PB_2 , *Appl. Phys. Lett.* **97**, 202504 (2010).
 - [3] M. A. McGuire and D. S. Parker, Magnetic and structural properties of ferromagnetic Fe_5PB_2 and Fe_5SiB_2 and effects of Co and Mn substitutions, *J. Appl. Phys.* **118**, 163903 (2015).
 - [4] T. N. Lamichhane, V. Taufour, S. Thimmaiah, D. S. Parker, S. L. Bud'ko, and P. C. Canfield, A study of the physical properties of single crystalline $\text{Fe}_5\text{B}_2\text{P}$, *J. Magn. Magn. Mater.* **401**, 525 (2016).
 - [5] A. Brauner, C. A. Nunes, A. D. Bortolozzo, G. Rodrigues, and A. J. S. Machado, Superconductivity in the new $\text{Nb}_5\text{Si}_{3-x}\text{B}_x$ phase, *Solid State Commun.* **149**, 467 (2009).
 - [6] A. J. S. Machado, A. M. S. Costa, C. A. Nunes, C. A. M. dos Santos, T. Grant, and Z. Fisk, Superconductivity in Mo_5SiB_2 , *Solid State Commun.* **151**, 1455 (2011).
 - [7] M. Fukuma, K. Kawashima, M. Maruyama, and J. Akimitsu, Superconductivity in W_5SiB_2 with the T_2 phase structure, *J. Phys. Soc. Jpn.* **80**, 024702 (2011).
 - [8] M. Fukuma, K. Kawashima, and J. Akimitsu, Superconducting state in $(\text{W,Ta})_5\text{SiB}_2$, *Phys. Procedia* **27**, 48 (2012).
 - [9] M. A. McGuire and D. S. Parker, Superconductivity at 9 K in Mo_5PB_2 with evidence for multiple gaps, *Phys. Rev. B* **93**, 064507 (2016).
 - [10] T. Shang, W. Xie, D. J. Gawryluk, R. Khasanov, J. Z. Zhao, M. Medarde, M. Shi, H. Q. Yuan, E. Pomjakushina, and T. Shiroka, Multigap superconductivity in the Mo_5PB_2 boron-phosphorus compound, *New J. Phys.* **22**, 093016 (2020).
 - [11] Y. Zhang, B. Wang, Z. Xiao, Y. Lu, T. Kamiya, Y. Uwatoko, H. Kageyama, and H. Hosono, Electride and superconductivity behaviors in Mn_5Si_3 -type intermetallics, *npj Quant. Mater.* **2**, 45 (2017).
 - [12] B. Cort, A. L. Giorgi, and G. R. Stewart, Low temperature specific heats of $\text{H}(\text{NbIrO})$ and $\text{R}(\text{NbPtO})$, *J. Low. Temp. Phys.* **47**, 179 (1982).
 - [13] S. Hamamoto and J. Kitagawa, Superconductivity in oxygen-added Zr_5Pt_3 , *Mater. Res. Express* **5**, 106001 (2018).
 - [14] T. Claeson, J. Ivarsson, and S. E. Rasmussen, Superconductivity of Nb_5Ge_3 , *J. Appl. Phys.* **48**, 3998 (1977).
 - [15] A. D. Bortolozzo, C. A. M. dos Santos, R. F. Jardim, C. Ritter, A. Devishvili, M. Rotter, F. G. Gandra, and A. J. S. Machado, Interstitial doping induced superconductivity at 15.3 K in Nb_5Ge_3 compound, *J. Appl. Phys.* **111**, 123912 (2012).
 - [16] S. T. Renosto, R. Lang, A. L. Manesco, D. Rodrigues, F. B. Santos, A. Machado, M. Baldan, and E. Diez, Strong electronic interaction and signatures of nodal superconductivity in $\text{Zr}_5\text{Pt}_3\text{C}_x$, *arXiv:1809.05008 [cond-mat.supr-con]* (2019).
 - [17] J. Kitagawa and S. Hamamoto, Superconductivity in $\text{Nb}_5\text{Ir}_{3-x}\text{Pt}_x\text{O}$, *JPS Conf. Proc.* **30**, 011055 (2020).

- [18] Y. Xu, S. Jöhr, L. Das, J. Kitagawa, M. Medarde, T. Shiroka, J. Chang, and T. Shang, Crossover from multiple- to single-gap superconductivity in $\text{Nb}_5\text{Ir}_{3-x}\text{Pt}_x\text{O}$ alloys, *Phys. Rev. B* **101**, 134513 (2020).
- [19] B. Lv, X. Y. Zhu, B. Lorenz, F. Y. Wei, Y. Y. Xue, Z. P. Yin, G. Kotliar, and C. W. Chu, Superconductivity in the Mn_5Si_3 -type Zr_5Sb_3 system, *Phys. Rev. B* **88**, 134520 (2013).
- [20] A. Bhattacharyya, P. P. Ferreira, K. Panda, S. H. Masunaga, L. R. de Faria, L. E. Correa, F. B. Santos, D. T. Adroja, K. Yokoyama, T. T. Dorini, R. F. Jardim, L. T. F. Eleno, and A. J. S. Machado, Electron-phonon superconductivity in C-doped topological nodal-line semimetal Zr_5Pt_3 : a muon spin rotation and relaxation (μSR) study, *J. Phys.: Condens. Matter* **34**, 035602 (2022).
- [21] A. A. Suter and B. M. Wojek, Musrfit: A free platform-independent framework for μSR data analysis, *Phys. Procedia* **30**, 69 (2012).
- [22] R. K. Harris, E. D. Becker, S. M. C. de Menezes, R. Goodfellow, and P. Granger, NMR nomenclature. Nuclear spin properties and conventions for chemical shifts, *Pure Appl. Chem.* **73**, 1795 (2001).
- [23] See Supplemental Material at <http://link.aps.org/supplemental/xxx> for details on the simulation of XRD patterns, the NMR data analysis, and the magnetic penetration depth.
- [24] X. Zhu, H. Yang, L. Fang, G. Mu, and H.-H. Wen, Upper critical field, Hall effect and magnetoresistance in the iron-based layered superconductor $\text{LaFeAsO}_{0.9}\text{F}_{0.1-\delta}$, *Supercond. Sci. Technol.* **21**, 105001 (2008).
- [25] N. R. Werthamer, E. Helfand, and P. C. Hohenberg, Temperature and purity dependence of the superconducting critical field, H_{c2} . III. Electron spin and spin-orbit effects, *Phys. Rev.* **147**, 295 (1966).
- [26] E. H. Brandt, Properties of the ideal Ginzburg-Landau vortex lattice, *Phys. Rev. B* **68**, 054506 (2003).
- [27] A. Yaouanc and P. D. de Réotier, *Muon Spin Rotation, Relaxation, and Resonance: Applications to Condensed Matter* (Oxford University Press, Oxford, 2011).
- [28] A. Amato, Heavy-fermion systems studied by μSR technique, *Rev. Mod. Phys.* **69**, 1119 (1997).
- [29] S. J. Blundell, Spin-polarized muons in condensed matter physics, *Contemp. Phys.* **40**, 175 (1999).
- [30] A. Maisuradze, R. Khasanov, A. Shengelaya, and H. Keller, Comparison of different methods for analyzing μSR line shapes in the vortex state of type-II superconductors, *J. Phys.: Condens. Matter* **21**, 075701 (2009), and references therein.
- [31] W. Barford and J. M. F. Gunn, The theory of the measurement of the London penetration depth in uniaxial type II superconductors by muon spin rotation, *Physica C* **156**, 515 (1988).
- [32] M. Tinkham, *Introduction to Superconductivity*, 2nd ed. (Dover Publications, Mineola, NY, 1996).
- [33] A. Carrington and F. Manzano, Magnetic penetration depth of MgB_2 , *Physica C* **385**, 205 (2003).
- [34] R. Kubo and T. Toyabe, A stochastic model for low field resonance and relaxation, in *Magnetic Resonance and Relaxation*, edited by R. Blinc (North-Holland, Amsterdam, 1967) pp. 810–823.
- [35] D. Massiot, F. Fayon, M. Capron, I. King, S. Le Calvé, B. Alonso, J.-O. Durand, B. Bujoli, Z. Gan, and G. Hoatson, Modelling one- and two-dimensional solid-state NMR spectra, *Magn. Reson. Chem.* **40**, 70 (2002).
- [36] W. A. Hines, L. T. Kabacoff, R. Hasegawa, and P. Duwez, NMR Knight shifts and linewidths in the NiPdP and NiPtP metallic glasses: Composition and temperature dependences, *J. Appl. Phys.* **49**, 1724 (1978).
- [37] I. Weisman and W. Knight, Satellite structure and NMR shift of ^{195}Pt in Pt-Mo alloys, *Phys. Lett. A* **25**, 546 (1967).
- [38] Y. Yafet and V. Jaccarino, Nuclear spin relaxation in transition metals; core polarization, *Phys. Rev.* **133**, A1630 (1964).
- [39] L. H. Bennett, R. E. Watson, and G. C. Carter, Relevance of Knight shift measurements to the electronic density of states, *J. Res. Nat. Bur. Stand.* **74A**, 569 (1970).
- [40] G. S. Carter, L. H. Bennett, and D. J. Kahan, *Metallic Shifts in NMR* (Pergamon Press, Oxford, 1977).
- [41] A. M. Clogston, A. C. Gossard, V. Jaccarino, and Y. Yafet, Orbital paramagnetism and the Knight shift in transition metal superconductors, *Rev. Mod. Phys.* **36**, 170 (1964).
- [42] N. Barbero, T. Shiroka, B. Delley, T. Grant, A. J. S. Machado, Z. Fisk, H.-R. Ott, and J. Mesot, Doping-induced superconductivity of ZrB_2 and HfB_2 , *Phys. Rev. B* **95**, 094505 (2017).
- [43] J. Bardeen, L. N. Cooper, and J. R. Schrieffer, Theory of superconductivity, *Phys. Rev.* **108**, 1175 (1957).
- [44] J. K. Jung, S. H. Baek, F. Borsa, S. L. Bud'ko, G. Lapertot, and P. C. Canfield, ^{11}B NMR and relaxation in the MgB_2 superconductor, *Phys. Rev. B* **64**, 012514 (2001).
- [45] H. B. Brom and J. Zaanen, Magnetic ordering phenomena and dynamic fluctuations in cuprate superconductors and insulating nickelates, in *Handbook of Magnetic Materials*, edited by K. H. J. Buschow (Elsevier, Amsterdam, 2003) pp. 379–496.
- [46] L. C. Hebel and C. P. Slichter, Nuclear relaxation in superconducting aluminum, *Phys. Rev.* **107**, 901 (1957).
- [47] T. Shang, D. Tay, H. Su, H. Q. Yuan, and T. Shiroka, Evidence of fully gapped superconductivity in NbReSi : A combined μSR and NMR study, [arXiv:2204.04365 \[cond-mat\]](https://arxiv.org/abs/2204.04365).
- [48] J. Korringa, Nuclear magnetic relaxation and resonance line shift in metals, *Physica* **16**, 601 (1950).
- [49] D. Pines, Electron interaction in metals, in *Solid State Physics*, Vol. 1, edited by F. Seitz and D. Turnbull (Academic Press, New York, 1955) pp. 367–450.
- [50] R. Prozorov and R. W. Giannetta, Magnetic penetration depth in unconventional superconductors, *Supercond. Sci. Technol.* **19**, R41 (2006).